A&A 550, A62 (2013)
DOI: 10.1051/0004-6361/201220413
© ESO 2013

Astronomy & Astrophysics

Extracting interstellar diffuse absorption bands from cool star spectra

Application to bulge clump giants in Baade's window

H.-C. Chen[1], R. Lallement[1], C. Babusiaux[1], L. Puspitarini[1], P. Bonifacio[1], and V. Hill[2]

[1] GEPI Observatoire de Paris, CNRS, Université Paris-Diderot, Place Jules Janssen, 92195 Meudon Cedex, France
e-mail: hui-chen.chen@obspm.fr
[2] Université de Nice Sophia Antipolis, CNRS, Observatoire de la Côte d'Azur, Laboratoire Cassiopée, BP 4229, 06304 Nice Cedex 4, France

Received 19 September 2012 / Accepted 5 November 2012

ABSTRACT

Aims. Interstellar (IS) absorption lines or diffuse bands are usually extracted from early-type star spectra because they are characterized by smooth continua. However, this introduces a strong limitation on the number of available targets, and reduces potential studies of the IS matter and the use of absorptions for cloud mapping.
Methods. We have developed a new and automated fitting method appropriate to interstellar (IS) absorptions in the spectra of cool stars that possess stellar atmospheric parameters. We applied this method to the extraction of three diffuse interstellar bands (DIBs) in high resolution VLT FLAMES/GIRAFFE spectra of red-clump stars from the bulge. By combining all stellar synthetic spectra, HITRAN-LBLRTM atmospheric transmission spectra and diffuse band empirical absorption profiles, we determined the 6196.0, 6204.5, and 6283.8 Å DIB strength toward the 219 target stars and discuss the sources of uncertainties. To test the sensitivity of the DIB extraction, we compared all three results and compared the DIB equivalent widths (EWs) with the reddening derived from an independent extinction map based on OGLE photometric data. We also derived the three independent color excess estimates based on the DIB strengths and average linear correlation coefficients previously established in the solar neighborhood and compared with the OGLE photometric results.
Results. Most stellar spectra could be reproduced well by the composite stellar, atmospheric, and IS models. Measurement uncertainties on the EWs are smaller for the broad and strong 6283.8 Å DIB, and are in the range 10−15%. Uncertainties on the two narrow and weaker DIBs are larger, as expected, and found to be highly variable from one target to the next. They strongly depend on the star's radial velocity. DIB-DIB correlations among the three bands demonstrate that a meaningful signal is extracted. For the 6284 and 6204 Å DIBs, the star-to-star variability of the EW also reflects features of the OGLE extinction map. The three independent extinction estimates deduced from the EWs and solar neighborhood correlation coefficients agree with each other within 20%, a value which probably reflects that they belong to different *families*. The estimated average color excess is also compatible with the photometric determination.
Conclusions. This work demonstrates the feasibility of the method of ISM DIB extraction in cool star spectra, based on synthetic spectra. It confirms that DIB measurements and local DIB-extinction calibrations can provide rough, first-order estimates of the towards distant targets.

Key words. ISM: lines and bands – dust, extinction – ISM: structure – ISM: molecules – stars: late-type – methods: data analysis

1. Introduction

Diffuse interstellar bands (DIBs) and interstellar (IS) absorption lines have been almost exclusively extracted from early-type star spectra, using the fact that stellar lines are broad, shallow, and limited in number, and that they do not contaminate the IS lines. The stellar continua can be easily fitted without any need for stellar models. However, extracting absorption from early-type star spectra is a strong limiting factor since it considerably reduces the number of potential targets, the information that can be obtained on the source regions of the absorptions, and especially the spatial resolution that can be achieved. In the case of the DIBs, it limits studies of the DIB response to the radiation field and to the local physical properties within the IS clouds, while such studies are promising tools in the search for the DIB carriers (e.g., Vos et al. 2011). Moreover, with the advent of stellar spectroscopic surveys at increasing resolution, the use of multi-object spectrographs and the perspective of forthcoming *Gaia* parallaxes, a large amount of line-of-sight integrated absorption data will become available.

Extracting absorption characteristics towards all targets, including cool stars, would allow better mapping of the galactic ISM, because it would considerably increase the achievable spatial resolution. For such mapping, IS lines of atoms, simple molecules, and DIBs are available, since all three contain information on the amount of IS matter. While the first two are well identified, carriers of the last remain unknown, despite their early discovery (e.g., Herbig 1995; Jenniskens & Desert 1994; Salama et al. 1996; Fulara & Krelowski 2000; Snow & Destree 2011; Friedman et al. 2011; Hobbs et al. 2008, 2009). Still, this lack of carrier identification and the fact that most of them are only weakly correlated with extinction or gas column are not incompatible with their use as tracers of IS clouds in the same way IS lines are used; i.e., the radial gradients of their strengths allow

locating IS clouds in distance and building 3D maps. In some respects, DIBs may have advantages as interstellar medium (ISM) tracers, because they are numerous, thus observable at various instrumental settings; they are often broad; and in general they are unsaturated. Recent data analyses suggest that the average ratios between the DIBs and the extinction do not seem to vary significantly within the first kiloparsec (Friedman et al. 2011; Vos et al. 2011). Finally, making use of cooler stars to extract their strengths reduces the dispersion around the average relationship, because extreme ionizing field effects linked to bright and hot targets are avoided (Raimond et al. 2012). For this reason, extracting DIB information from cool stars would be another improvement to the mapping.

Here we present a new method of DIB measurement based on cool star synthetic spectra, and as a test case we applied this technique to three different diffuse bands and 219 targets located in the Galactic bulge that have the advantage of possessing precise determinations of their atmospheric parameters. We selected the 6196.0, 6204.5, and 6283.8 Å DIBs that are the three strongest absorptions contained in the observed spectral interval. Those DIBs have already been widely studied (see e.g., the works of Galazutdinov et al. 2008; Cami et al. 1997; Friedman et al. 2011; Vos et al. 2011). We estimate the statistical and systematic uncertainties on the DIB equivalent widths (EWs) and discuss potential improvements. We compare the measured EW angular pattern over the field with an independent mapping of the reddening based on photometric data of stars close to the Galactic center (GC). We finally use average DIB-reddening empirical relationships previously established in the Sun's vicinity to derive three independent estimates of the reddening towards all targets, compare the three estimate together, and finally compare with the photometric determination.

This article is organized as follows. Data are presented in Sect. 2. In Sect. 3 we describe the new method of IS absorption band extraction and its ingredients. In Sect. 4, we show the model adjustments for selected target stars and discuss the results. In Sect. 5, we discuss the relations between the DIBs and between the DIBs and the extinction obtained by photometry. Section 6 presents color excess estimates based on the DIBs and nearby star studies. Finally, we summarize the results and discuss the perspectives in the last section.

2. Data

We used the sample of 219 bulge red clump giants of Hill et al. (2011). Those stars were observed with FLAMES/GIRAFFE at the VLT and are located within a 12 arcmin radius field in Baade's Window ($l = 0.8$, $b = -4$). We used here the spectra obtained with the GIRAFFE HR13 setup, leading to a resolution of $R = 22\,500$ and a spectral coverage spanning 6120 to 6405 Å, which contains three well known diffuse bands. The target selection, observations, data reduction, and stellar-parameter determination are described by Hill et al. (2011). Those stellar parameters were determined by these authors from photometric and spectroscopic data. Here we use the effective temperature, gravity, micro-turbulence, and metallicity resulting from their analysis, whose full ranges for the present sample are listed in Table 1. The different exposures were observed within a week interval so that at this resolution we can neglect variations in the radial velocity difference between the telluric and stellar lines and work with the final co-added spectra. Signal-to-noise ratios vary between ≃30 and 77 per pixel. (The Giraffe pixel-size is 0.07 Å.)

Table 1. Stellar parameters.

Parameters	Min	Max	Unit
$T_{\rm eff}$	4270	5448	K
$\log g$	1.97	2.46	
$v_{\rm t}$	0.8	1.8	km s^{-1}
[Fe/H]	−1.13	0.71	

Notes. $T_{\rm eff}$ is the effective temperature. $\log g$ is the gravity. $v_{\rm t}$ is the micro-turbulent velocity. [Fe/H] is the metallicity.

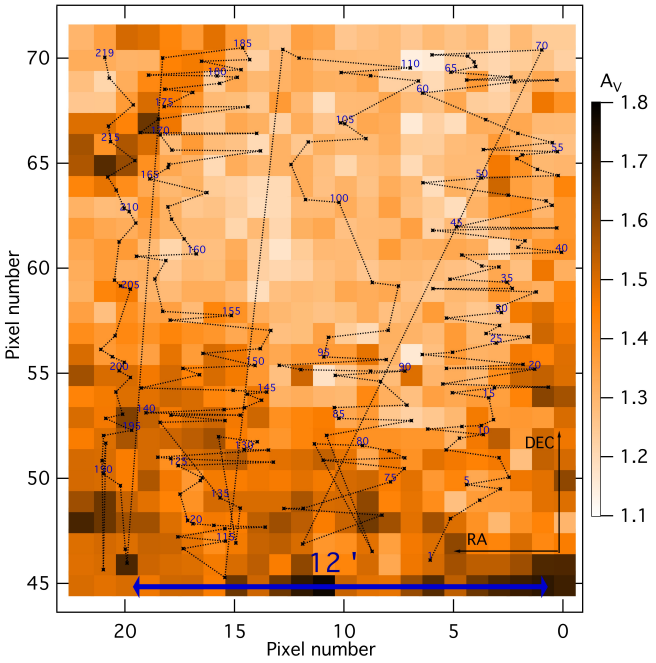

Fig. 1. Target stars used in this study (black crosses) superimposed on the extinction map from Sumi (2004). The map is centered on (l, b) = (0.8, −4). Each pixel is 0.6′ × 0.6′. The extinction scale is displayed in Fig. 14. Stars are numbered according to Table 3. Dotted lines link stars in increasing order of their ID number. Only one out of five numbers is indicated for clarity.

This region benefits from a high-resolution differential extinction map that was derived from the OGLE-II red clump giants photometry by Sumi (2004). Assuming a mean reddening-corrected color for the red clump, Sumi (2004) divided each field in small subfields, computed the mean observed color of the red clump in each subfield and derived the reddening E_{V-I}. The resulting extinction map has a spatial resolution of 33 arcsec in our field. For comparison purposes we have interpolated within the Sumi (2004) reddening grid to infer its value at each target location. Sumi (2004) indicates a potential zero-point offset for A_v that may amount to 0.05. The distribution of the target stars is shown superimposed on the Sumi (2004) extinction map in Fig. 1.

3. Fitting procedure

Our approach is to model and adjust the spectrum of the background star, the DIB, and the atmospheric transmission simultaneously in one unique step. In the opposite case of hot stars, extracting the IS absorption was done in two or three steps. The correction for the telluric absorption, if necessary, was done first and independently of the IS absorption fitting. Synthetic

transmission spectra were adjusted through computing the mean ratio between observed and modeled EWs of specific lines (Lallement et al. 1993), or by minimizing the length (defined as the sum of flux differences between consecutive points) of the residual spectrum obtained after dividing by the model atmospheric transmission (Raimond et al. 2012). None of those methods is necessary here, since the atmospheric transmission model is adjusted in velocity and airmass during the global adjustment. In a second step the smooth continuum of the hot star was fitted to a function, and in a last step the DIB strength was measured using the normalized spectrum. Characterizing the DIB strength was done in several ways, the two main ones being measurements of the central depth and of the EW. We refer to the detailed discussion of this point by Friedman et al. (2011). We chose here the EW, and, as we will see, this is the quantity that comes directly out from our cool star analysis.

For cool stars, the presence of numerous, deep, and narrow stellar lines precludes applying the simple continuum fitting procedure that is used for stars of earlier spectral types. Identifying and correcting the stellar lines one by one in the IS absorption region is not practical. Furthermore, if the stellar lines and the IS absorption do overlap, it is very difficult or even impossible to separate them, hence our approach using a global adjustment. Our composite model here is the product of a synthetic stellar spectrum, a synthetic telluric transmission, and an empirical model for the DIB absorption. The model allows for wavelength shifts between those three spectra to take the stellar radial velocity, the Earth motion, and the IS radial velocity into account. The giant stars used as background sources in the present investigation do not have measurable projected rotational velocities at this resolution. Sizeable projected rotational velocity in the background star could be modeled as well, if necessary. The combination of the three models is convolved by a Gaussian profile to take the instrumental spectral resolution into account and is adjusted to the data in the DIB region, with the DIB strength, the DIB center location, and an atmospheric transmission scaling (see below) as the free parameters.

The synthetic stellar spectra, $S(\lambda)$, were computed from an ATLAS 9 model atmosphere using the SYNTHE suite (Kurucz 2005). We used the Linux port of all the codes (Sbordone et al. 2004; Sbordone 2005). Atomic and molecular data were taken from the data base on Kurucz's website[1] (Kurucz 2005). For each star we computed a synthetic spectrum with the stellar parameters obtained by Hill et al. (2011), i.e. the effective temperatures, gravity, metallicity, and microturbulence, summarized in Table 1. The stellar radial velocity is taken into account by Doppler-shifting the computed spectrum to the appropriate radial velocity.

The synthetic telluric transmissions were computed by means of the LBLRTM code (Line-By-Line Radiative Transfer Model, Clough et al. 2005), using the molecular database HITRAN (HIgh-resolution TRANsmission molecular absorption, Rothman et al. 2009). Here we have used the transmission $T_0(\lambda)$ computed for a standard atmosphere and for the altitude of the observatory and assumed that airmass variations from star to star simply result in a variable coefficient α for the transmission, with $T(\lambda) = T_0(\lambda)^\alpha$. The projected Earth motion is taken into account by Doppler-shifting the transmission.

Finally, the profiles of the 6196.0, 6204.5, and 6283.8 Å DIBs are derived from a high resolution ($R = 48\,000$), high signal-to-noise survey of early-type stars recorded with the FEROS spectrograph at the 2.2 m ESO/Max Planck Institute Telescope in La Silla. Those profiles do not reveal the fine structure that is known to be present Galazutdinov et al. (2008), but this is not necessary here since we deal with spectra at a resolution that is lower than the one of FEROS. The shape of the 6283.8 Å DIB, which is contaminated by strong telluric molecular oxygen lines, has been derived by Raimond et al. (2012) by averaging a large number of individual shapes obtained after division by an adjusted telluric template. This use of a synthetic atmospheric model is allowed by this DIB being relatively strong and much broader than the telluric lines. In the same way, this DIB is broader here than the stellar lines and thus relatively easy to detect and measure (see Figs. 3–5). The two, much weaker DIBs, 6196.0 and 6204.5 Å, are in regions that are free of contaminating telluric lines. Their shapes were derived by means of an automated fitting method appropriate to early-type stars (Puspitarini et al. 2012, priv. comm.). About ten individual profiles extracted from the best FEROS spectra were averaged to produce those templates. Since those two DIBs are narrower than the 6283.8 Å DIB, here in the case of cool stars they are much more difficult to measure due to the overlap with the similarly narrow stellar lines.

Neglecting emissions from the cloud in comparison with the stellar flux, DIB transmission profiles $D(\lambda)$ can be expressed as $\exp(-\tau(\lambda))$, where $\tau(\lambda)$ is the optical thickness as a function of wavelength. The value of $\tau(\lambda)$ is proportional to the column N of absorbers and can be expressed as $\tau(\lambda) = N/N_0\tau_0(\lambda)$, $\tau_0(\lambda)$ and N_0 being some related optical thickness and column of reference. Calling β the N/N_0 ratio, a quantity proportional to the column density of the DIB carrier, one has $D(\lambda) = D_0(\lambda_D)^\beta$, where $D_0(\lambda) = \exp(-\tau_0(\lambda))$ is the reference profile derived from the FEROS analyses, and λ_D is the wavelength shifted by the radial velocity of the main absorbing medium. The DIB EW is, by definition,

$$W = \int \frac{I_0(\lambda) - I(\lambda)}{I_0(\lambda)} \mathrm{d}\lambda = \int (1 - \exp(-\tau(\lambda))) \mathrm{d}\lambda \quad (1)$$

where $I_0(\lambda)$ and $I(\lambda)$ are the unabsorbed and absorbed intensities. Within the weak absorption regime appropriate here, τ is small, $\exp(-\tau) \simeq 1 - \tau$ and the EW W is approximated by

$$W = \int \tau(\lambda) \mathrm{d}\lambda = \int \beta\tau_0(\lambda) \mathrm{d}\lambda = \beta W_0 \quad (2)$$

where W_0 is the EW of the line of reference.

We chose to list the results in the form of the product βW_0, which has the advantage of being both truly proportional to the absorbing column and being an equivalent width, i.e., a widely used, meaningful quantity. For the broader DIB, 6284 Å, the relative difference between βW_0 and the actual EW is smaller here than 4.5%, a value reached for EWs on the order of 1.2 Å. For the narrower DIB, 6196 Å, the departure from the linear regime for the EW occurs at a smaller optical thickness; however, the DIB is weak, and finally the relative difference between βW_0 and the actual EW is less than 4%, a value reached for EWs on the order of 70 mÅ.

After adjusting the coefficient β through spectral fitting, the DIB EW is thus simply computed as the product of the EW of the reference profile W_0 by the coefficient β. We also assume here that most of the absorbing medium originates in clouds with a similar radial motion, or equivalently that the DIB is negligibly broadened by the line-of-sight velocity structure. This assumption is legitimated here by the fact that most of the absorption arises within 1500 pc from the Sun, as derived from the extinction model of Marshall et al. (2006) and that for those low l, b

[1] http://kurucz.harvard.edu

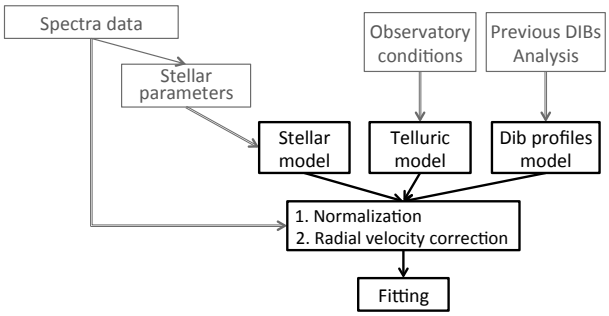

Fig. 2. Procedure flowchart of the fitting.

coordinates the projection of the gas motions onto the line-of-sight remains small with respect to the DIB spectral width.

Figure 2 illustrates the procedure for this study. The stellar parameters are used as input for the stellar synthetic models, and the stellar radial velocity is taken into account by an appropriate shift. The atmospheric synthetic model of reference is calculated based on the position and altitude of the observatory. While doing the fitting, the program computes the product $\kappa\ S(\lambda_S)\ T_0(\lambda_E)^{\alpha}\ D_0(\lambda_D)^{\beta}$, with κ being a scaling factor, λ_S is the wavelength shifted by the stellar radial velocity, λ_E by the Earth's radial velocity and λ_D by the radial velocity of the DIB absorbing medium, and convolves the product of the three models by a Gaussian instrumental function appropriate for the resolution of GIRAFFE.

Telluric absorptions should be identical for all fibers for the same exposure, and we also expect the DIB radial velocity to vary very little over the narrow field. Still, to test the adjustment and allow for small uncertainties in the three wavelength shifts, we started by allowing all parameters κ, α, β, λ_S, λ_E and λ_D to freely vary, and performed a least mean squares adjustment to the data for each star. All the fittings were done in an automated way. The results revealed a large majority of identical or very close values for the λ_E shift (actually a null value for a fit in the earth frame) and for α. As mentioned previously this was expected for both α, which responds to the airmass, and λ_E, a function of the date. We extracted those two parameters and kept them fixed for the second adjustment phase. From this first attempt we could also check that the values found by fitting for λ_S differ from the radial velocities from Hill et al. (2011) by very small velocity intervals (on the order of 1 km s^{-1}). We kept those very small differences from values in Table 3 and fixed λ_S for the next step. Finally, the coefficient λ_D that represents the DIB shift was also found to be the same or nearly the same for a large majority of the stars. This confirms that the DIB radial velocity variation is very small over such a small field of view, both because most of the absorption originates in the first two kpc, and also because the radial motion of the absorbing gas in this direction is small. We then fixed this shift λ_D at the most frequently found value. For all those four parameters we checked that the outliers correspond to low signal-to-noise spectra or to the presence of a spurious feature. We then proceeded to a second fit of all spectra, this time only for free κ and β coefficients.

4. Model adjustments

Figures 3–9 illustrate exemplary cases of model adjustments for the three 6196.0, 6204.5, and 6283.8 Å DIBs chosen for this study.

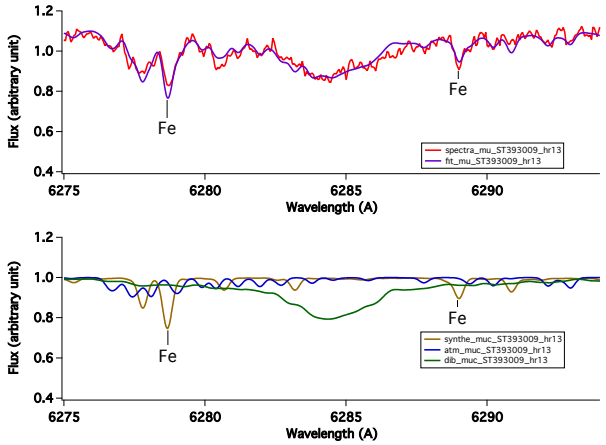

Fig. 3. Model adjustment for Ogle N: 393009 ($T_{\rm eff}$ = 5012 K). The DIB is in a region devoid of strong stellar lines. The *upper panel* shows the spectrum (red line) and the best-fit model (purple line). The *lower panel* shows the synthetic stellar model (yellow line), the synthetic atmospheric model (blue line), and the DIB profile (green line), which all correspond to the fit parameters.

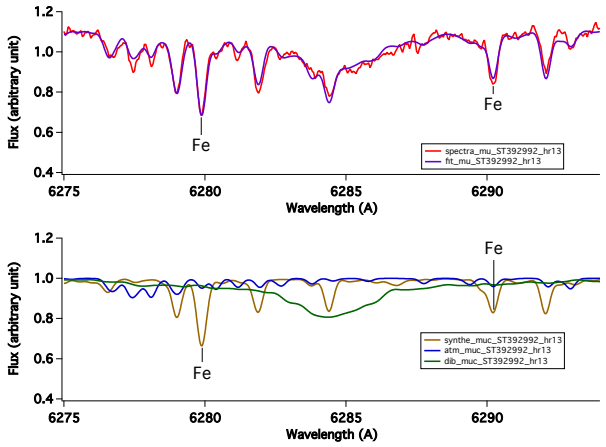

Fig. 4. Same as Fig. 3 for Ogle N: 392992 ($T_{\rm eff}$ = 4907 K). The DIB here is in a spectral region characterized by moderately strong stellar lines.

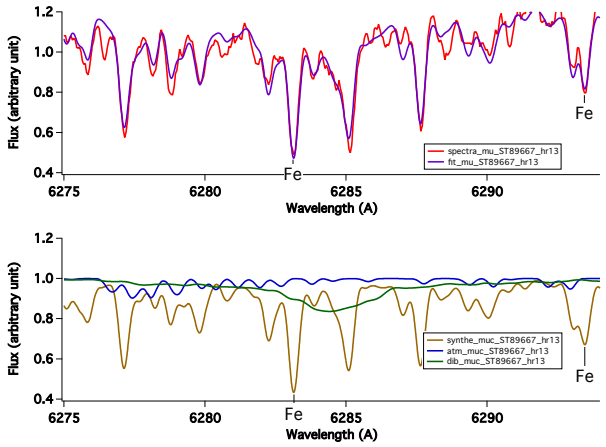

Fig. 5. Same as Fig. 3 for Ogle N: 89667 ($T_{\rm eff}$ = 4516 K). The DIB here is both weak and embedded in strong stellar lines.

What we aim at showing in those figures are the strong differences linked to the target star individual radial velocities, which vary over a very large velocity interval, from −230 to +250 km s^{-1}. This results in very different locations of the DIBs with respect to the main stellar lines. There are also very large differences between the 6283.8 Å DIB and the two narrow ones, with a much stronger impact of the star radial velocity and of the signal-to-noise on the DIB detection for the last two DIBs. Finally, the higher the metallicity, the stronger the stellar lines and their impact on the DIB measurement, especially again in the case of the two narrow and weak DIBs.

Figures 3 to 5 show three examples of adjustments for the strongest and broadest DIB at 6283.8 Å, The first star (Fig. 3) corresponds to an optimal case: given the star radial velocity, only weak stellar lines are located in the DIB region, and the fitting program could easily adjust the DIB strength. Moreover, the star is metal-poor (Fe/H = −0.68), which helps the fitting procedure further. Figures 4 and 5 correspond to more difficult cases, with one or more strong stellar lines in the DIB region. In those cases, it should be possible to measure the DIB strengths with accuracy, provided the stellar models adequately predict the stellar line depths. However, it can be seen that there are significant and often systematic differences between the observed and modeled lines for some spectral regions. Such departures may have several origins: the oscillator strengths (log(gf)) and other atomic data (wavelengths, damping constants) that we use have an error attached to them; some of the lines are simply not identified and absent from our line list; our spectra are computed assuming local thermodynamic equilibrium (LTE); departures from LTE in the stellar atmosphere may change the line strength, for a given abundance; the model atmospheres we used are one-dimensional static and plane-parallel, hydrodynamic effects (granulation) may also affect both the line strengths and shapes. In practice our computed stellar spectrum differs from the observed spectrum due to a number of shortcomings in our modeling. For example, significant residuals are found at the locations of unidentified lines of the solar spectrum, such as the 6273.949, 6282.816, 6286.142, and 6288.315 Å lines (Moore et al. 1966). Obviously such unidentified lines are not present in our line list. Details on these discrepancies can be found in the Appendix, which aims at estimating the uncertainties on the DIBs EWs and at empirically correcting for systematic effects. Nevertheless, despite the observed departures from the stellar model, the DIB is broad enough here for a reliable DIB estimate. Figure 5 illustrates this property, and shows one of the worst cases of overlapping stellar lines, a metal-rich (although moderately, Fe/H = 0.67) target star, and one of the smallest DIB EWs. The DIB strength could be measured reasonably well despite those conditions, thanks to the good signal-to-noise ratio of the spectrum and the width of the DIB.

This is not the case for the two narrow DIBs. Figures 6 to 9 show two examples of determinations for each of the 6196.0 and 6204.0 Å DIBs, a relatively *easy* one with only weak stellar lines contaminating the DIB region, and a *difficult* one with stellar lines overlapping the DIB. In the first case, it can be seen that DIB EWs can be safely measured. In the second, it is clear from the figure that the stellar line accuracy is critical and that some of the measurements are very uncertain, at least for the low extinction (and DIB strength) regime that prevails here. In comparison with those uncertainties, additional errors linked to the use of a predefined shape of the DIB, as well as to the telluric model (for the 6284 Å DIB), are negligible. Those systematic departures have been studied in detail and are discussed in the Appendix.

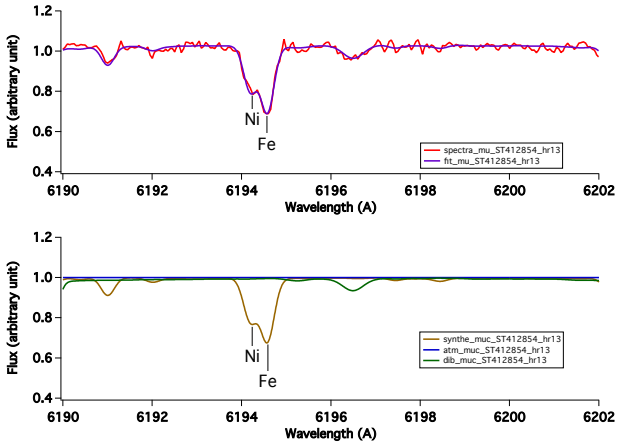

Fig. 6. Same as Fig. 3 for the 6196 Å DIB and Ogle N: 412854 ($T_{\rm eff}$ = 5191 K). The narrow DIB is in a region devoid of strong stellar lines.

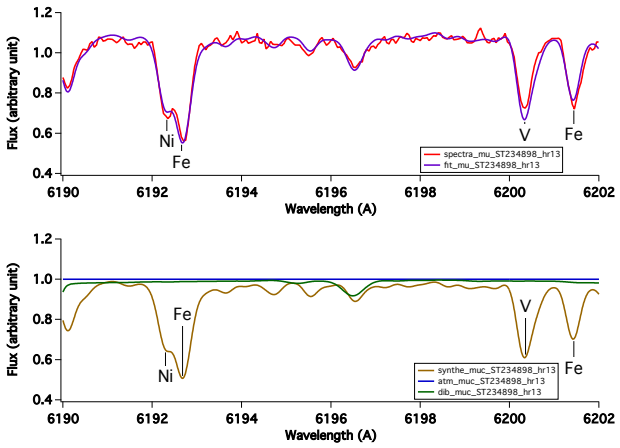

Fig. 7. Same a Fig. 6 for Ogle N: 234898 ($T_{\rm eff}$ = 4714 K). The DIB and a strong stellar line do overlap.

Based on them, a first-order empirical correction was devised and was applied to the DIB derivation. In brief, residuals for all spectra were all shifted to the stellar frame, and the resulting spectra were sorted as a function of the stellar metallicity (see Fig. A.1 in the Appendix). At each wavelength an average linear relationship between the residual value and the metallicity was adjusted, providing a systematic offset as a function of metallicity and wavelength (Figs. A.2 and A.3). This offset is maximal at the locations of the over- or underpredicted lines, and nil elsewhere. Such an offset was then applied as a corrective term at all wavelengths to all DIB spectra (Fig. A.4), and a new adjustment of the model and subsequent computation of the DIB EW were performed after those corrections. We compared the DIB-DIB relationships and also the DIB-extinction relationships both before and after the empirical correction, and found a systematically better DIB-DIB relationship, in particular with a factor of two increase in the Pearson correlation coefficient in the case of the 6196 Å vs. 6204 Å DIB comparison. We also found a significant improvement in the DIB-extinction relationship, except for the 6284 Å DIB for which there was no change. We are conscious that a more fundamental approach would be desirable, but, in view of those improvements, we kept the corrected values for the remaining part of the analysis. More improvements

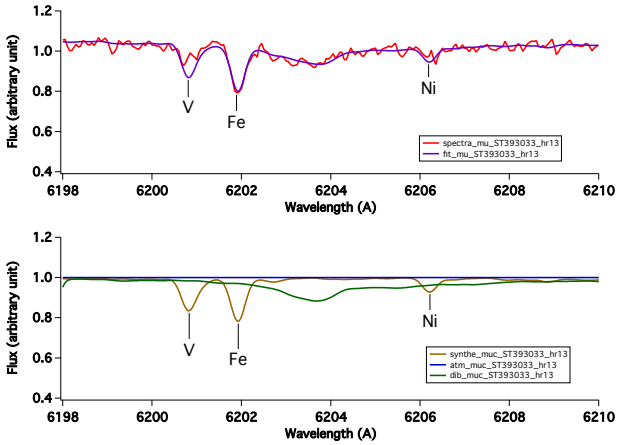

Fig. 8. Same as Fig. 3 for the 6204 Å DIB and Ogle N: 393033 ($T_{\rm eff}$ = 4914 K). The narrow DIB is in a region devoid of strong stellar lines.

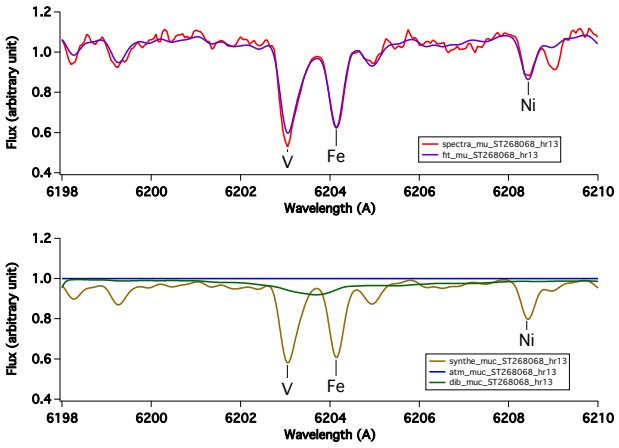

Fig. 9. Same as Fig. 8 for Ogle N: 268068 ($T_{\rm eff}$ = 4837 K). The DIB region corresponds to strong stellar lines.

are expected in future from elaborated studies of the stellar spectra in the DIB spectral regions, i.e. individual adjustments of the $\log(gf)$, studies of the missing lines, non-LTE and granulation effects. Such studies are beyond the scope of this work, which is devoted to testing the new method adapted to cool stars.

5. DIB equivalent widths, DIB-DIB, and DIB-extinction correlations

Table 3 lists the resulting EWs for the three DIBs, both before and after the empirical correction, as well as the associated uncertainty. Uncertainties, whose derivations are also described in detail in the Appendix, are a combination of random errors associated to the noise level and of errors linked to the use of the three models that remain after applying the above-mentioned empirical correction. These quasi-random uncertainties were derived from the whole set of residual vs metallicity curves that were computed for each wavelength and used for correcting of systematics. They were simply taken as the variance of the residuals around the mean relationship (see Figs. A.1 and A.2). This variances includes both the noise and the departure from the empirical *ideal* relationship between the metallicity and the stellar lines. It is clear that those derived uncertainties provide an order

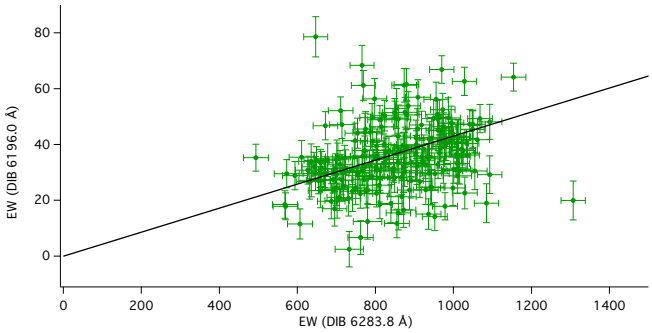

Fig. 10. Equivalent width (EW) of DIB 6196.0 Å as a function of the EW of DIB 6283.8 Å. The black line is the best linear fit for pure proportionality, using error bars of both DIBs.

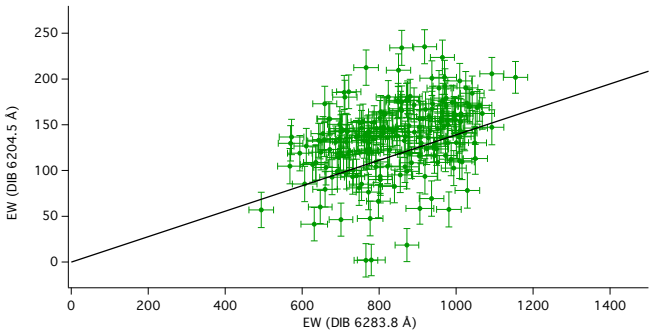

Fig. 11. Same as Fig. 10 for DIB 6204 Å.

of magnitude of the errors, which has a sense as a mean for all targets, but that individual errors for each target may be larger or smaller. Future work will address this point, once additional studies of the stellar models have been performed.

An immediate test of the reliability of the DIB strengths is the existence of DIB-DIB correlations, because EWs have been measured independently for the three bands. This test is not so easy here owing to the limited range of extinctions (Sumi 2004). Still, the Spearman's rank correlation statistics allows the absence of two-by-two correlations to be rejected by better than 99.9%. Figures 10 and 11 show the DIBs 6196.0 and 6204.5 EWs as a function of the broad 6283.8 Å EW for the whole sample. The black lines correspond to a pure proportionality. Despite the large uncertainties, especially for the two small DIBs, the correlation between the three bands is clearly visible. Those correlations show that the signal we extracted for the DIBs contains some information on the IS absorption, even for the two small DIBs. A second test of the DIB measurement is obtained from a comparison with the extinction map. Figure 12 displays the star-by-star variations in each DIB EW, as well as the extinction derived from the OGLE photometry obtained by interpolation through the A_v map of Sumi (2004). The four patterns, which represent variations across the field of the four independent quantities, reveal large similarities for the strong DIB and some similarities for the 6204 Å DIB. Large uncertainties make the comparison less obvious for the 6196 Å band. This is reflected in the Spearman's rank correlation statistics that allow rejecting the absence of correlation at better than 99.9% for the 6284 and 6204 DIBs, and 90% for the 6196 Å DIB.

More precise statistics could have been obtained after rejections of the noisy spectra or particularly poor adjustments. However, our goal here is to provide some idea of the DIB

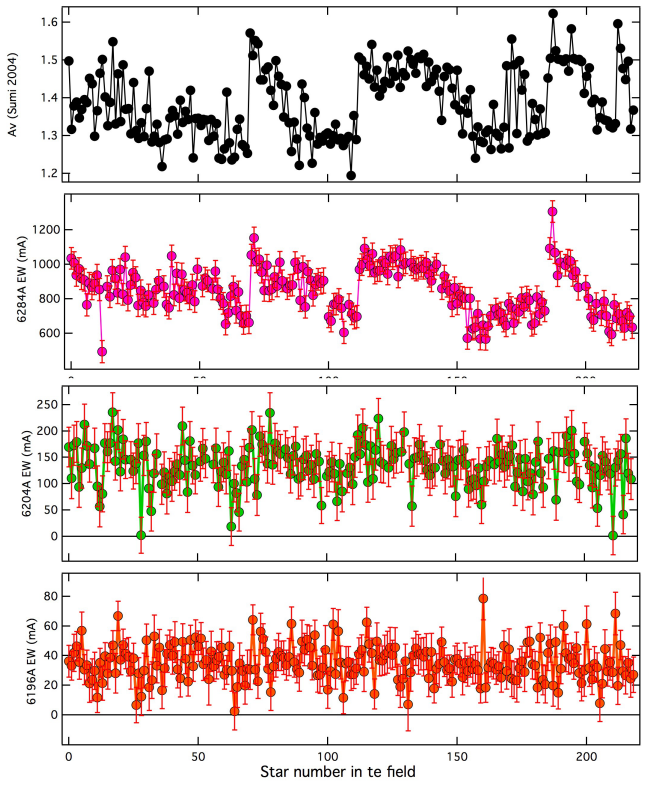

Fig. 12. From bottom to top, EWs of the three DIBs (6196, 6204, and 6284 Å) as a function of the star number and the extinction A_v interpolated from the map of Sumi (2004) at each star location.

extraction results as a function of the signal quality, the DIB strength, and the reddening for an entire field, with an entirely automated method.

6. Color excess estimates based on nearby star empirical relationships

Diffuse interstellar bands are moderately or only weakly correlated with the extinction, as shown by a number of studies and the existence of DIB *families* whose members are internally closely correlated, while distinct families seem to obey different laws (e.g., Krelowski & Walker 1987; Cami et al. 1997). There is no *parental* link between the three DIBs we study here, and thus we do not expect to find strong correlations between their EWs or very similar dependencies on the extinction. Previous surveys of stars in the solar neighborhood have provided some statistical relationships between the reddening E_{B-V} derived from spectrophotometry and the EW of each DIB. Best-fit parameters of linear correlations have been established recently by Friedman et al. (2011) for all three DIBs, based on about 130 O-B nearby northern hemisphere stars within 1 kpc. In the case of the 6284 Å DIBs, Raimond et al. (2012) derived slightly different coefficients based on about the same number of southern hemisphere targets, observed with the ESO/La Silla FEROS spectrograph. Using the same FEROS data, Puspitarini et al. (2012, priv. comm.) derived linear fit coefficients for the two other DIBs, again found to be slightly different when compared to the northern survey study. The coefficients for the linear relations between EW and E_{B-V} are shown in Table 2 for both surveys and for the three DIBs. There are some differences between the relationships as they emerge from the two surveys, which have been discussed by Raimond et al. (2012). Owing to

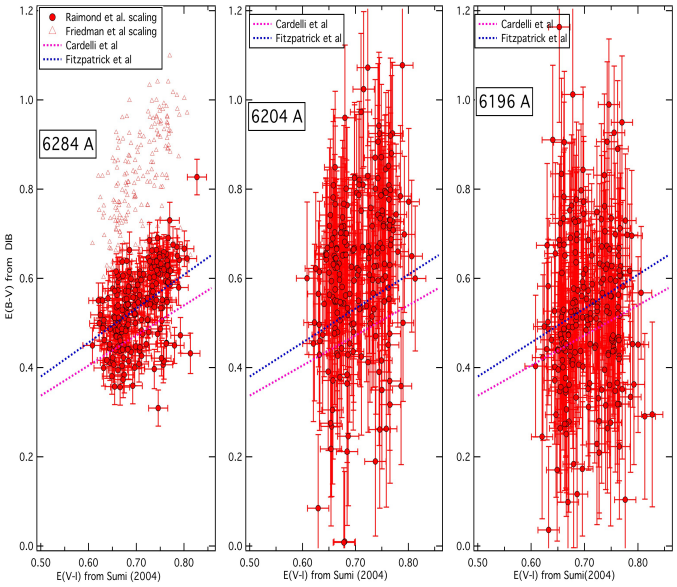

Fig. 13. Color excess E_{B-V} derived from the three DIBs as a function of the E_{V-I} value interpolated within the Sumi (2004) map at the locations of the target stars. E_{B-V}s here are obtained using the Raimond et al. (2012) and Puspitarini et al. (2012, priv. comm.) average relationships based on FEROS data. The blue and pink dotted lines correspond to color excess relationships based on the Fitzpatrick (1999) and Cardelli et al. (1989) extinction curves and $R_v = 3.1$ (see text). In the case of the DIBs 6283.8 Å we also show the color excess values deduced from the Friedman et al. (2011) average relationships (open triangles).

Table 2. Value of $E_{B-V,\lambda} = a + b \times EW_\lambda$.

DIB_λ	Reference	a	b
6196.0	1	$(-5.07 \pm 0.56) \times 10^{-2}$	$(2.11 \pm 0.02) \times 10^{-2}$
	2	0	$(1.48 \pm 0.09) \times 10^{-2}$
6204.5	1	$(-7.22 \pm 0.67) \times 10^{-2}$	$(5.99 \pm 0.08) \times 10^{-3}$
	2	0	$(4.58 \pm 0.37) \times 10^{-3}$
6283.8	1	$(-7.71 \pm 0.78) \times 10^{-2}$	$(9.57 \pm 0.17) \times 10^{-4}$
	3	$(-0.50 \pm 0.40) \times 10^{-2}$	$(6.37 \pm 0.23) \times 10^{-4}$

References. 1: Friedman et al. (2011); 2: Puspitarini et al. (2012, priv. comm.); 3: Raimond et al. (2012).

the use of cooler and fainter target stars, the ESO/FEROS DIB strengths are not as influenced by strong radiation fields, and there is significantly less dispersion around the mean DIB-E_{B-V} relationship. As a matter of fact, DIB strengths may be significantly reduced in case the main dust cloud responsible for the absorption is very close to the UV-bright target star (Friedman et al. 2011; Vos et al. 2011), an effect attributed to the ionization state change of the carriers in the stellar environment. For this reason, the number of *outliers* with a relatively weak DIB and a large reddening is smaller in the FEROS survey, and the dispersion decreases. In parallel, the mean slope E_{B-V}/EW(DIB) derived from the sample is also smaller. This was found systematically for the three DIBs. Here we make use of the FEROS-based mean relationships, because the line-of-sight here is not related to hot bright stars and the DIB should correspond better to average conditions. For comparisons we also show both results for the strong 6284 Å band.

The measured DIB EWs derived from the global fitting were converted into E_{B-V} color excess values by application of the three average relationships listed in Table 2.

Figure 13 shows the color excess E_{B-V} estimate based on the DIB 6283.8 Å and the FEROS relationship, as a function of the color excess E_{V-I} interpolated from the Sumi (2004) maps (x-axis). The figure is somewhat redundant with the previous one, however it provides a better idea of the EW dispersion and the global relationship. The data point distribution shows a correlation between the DIB-based and photometric determinations, but there is a large dispersion, and also the observed interval for the DIB strength is significantly larger than the range of variation in the photometric determination. (The best fit linear relationship does not go through zero.) The relationship between E_{B-V} and E_{V-I} depends on the extinction curve, and to a lesser extent on the stellar spectrum. We have drawn here the relationships based on both classical Cardelli et al. (1989) and Fitzpatrick (1999) extinction curves, for the total-to-selective extinction ratio $R_v = 3.1$. The value of E_{V-I} is computed for a typical red-clump giant star, and E_{B-V} is computed for the A0 star Vega. As far as average absolute values are concerned, the DIB-based E_{B-V}s are similar to what one would expect from those classical laws, and in better agreement with the Fitzpatrick relationship. We also show the E_{B-V} values we would obtain with the empirical Friedman et al. (2011) relationship. Those E_{B-V} empirical estimates are systematically higher and more difficult to reconcile with the photometric data. We believe that the relationship based on the cooler FEROS targets may be more appropriate here because it probes environmental conditions that are closer to the average conditions encountered here than to the high ionization conditions encountered towards O- and early B-type nearby target stars.

Figure 13 also shows how the 6196 and 6204 Å DIB-based color excess E_{B-V} compares with the photometric determination of E_{V-I}. For those two DIBs, the correlation is visible, and the agreement between the measured and the expected ratio between the two color excess values is again better with the Fitzpatrick (1999) reddening law. There appears to be less deviation from average simple proportionality for those DIBs, compared to 6284 Å, especially for the DIB 6196 Å for which the best-fit relationship is compatible with proportionality within the uncertainty range.

An important source of dispersion is the fact that the Sumi color excess is an average over the series of stars contained within the 0.6×0.6 arcmin pixel field and located at various distances in the bulge, while the DIB is derived for individual stars. Here the main effect would be angular variability, because, as said above, the quasi-totality of the extinction is generated closer than 2000 pc, thus differences in the distances to the bulge targets have in principle no impact. At 1 kpc, 0.6 acrimony corresponds to a transverse distance of 0.17 pc, thus only very dense, small cloud cores could produce variations as large as those observed. A likely explanation for both the dispersion and also departures from proportionality between the DIB-based color excess and the photometric E_{V-I} is the existence of intrinsic DIB variations in response to the radiation field and in general to environmental conditions, such as those found at smaller distances. This is favored by the spatial pattern as we discuss below. On the other hand, spatial variations of the DIB-E_{V-I} ratio may also be related to spatial variability of the extinction curve. Udalski (2003) and Sumi (2004) both consider R_v may vary significantly towards the bulge. A relationship between the extinction curve, the total to selective extinction ratio and the DIB behavior has been first discussed by Krełowski et al. (1999). Environmental effects and dust processing, on one hand, and extinction curve, on the other, are themselves related through the grain distribution and the cloud history, which also influences DIB carriers and strengths.

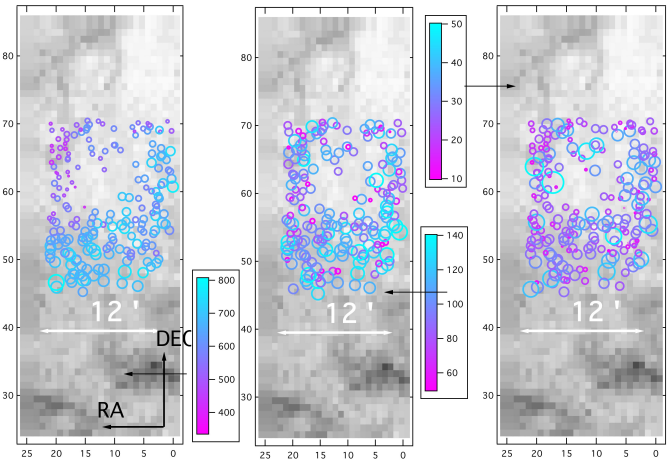

Fig. 14. Spatial variability of the DIB and the DIB-extinction ratio (from left to right, the 6284, 6204, 6196 Å DIBs). Target stars used in this study are superimposed on the A_v extinction map from Sumi (2004) (gray scale). The size of the circle is proportional to the DIB EW, and its color corresponds to the ratio between the DIB EW and the extinction A_v obtained by interpolation through the Sumi map (color scale).

The spatial variability of the ratio between DIB-based and photometric determinations of the color excess is shown superimposed on the Sumi map in Fig. 14. In this figure the color indicates the ratio and the size of the markers is proportional to the DIB strength. The distribution of colors shows that there are some systematic changes across the field for the 6284 DIB; in particular, the DIB is relatively small compared to the photometric value at larger declinations and right ascensions. Future investigations will hopefully allow those differences to be attributed in variations of the environmental conditions in the encountered clouds, to extinction law spatial variations, or both, as discussed above. The 6204 Å DIB shows the same behavior as the 6284 band, although less clearly, due to large uncertainties and also not as pronounced. At variance with the other two bands, the 6196 Å DIB does not reveal any spatial trend, although there are strong uncertainties on the DIB EW. If confirmed, for the three DIBs the spatial homogeneity of the measured ratio follows the degree of correlation of the DIBs with the color excess, as measured in the solar neighborhood and for widely distributed targets by Friedman et al. (2011). The correlation degree and spatial homogeneity decrease from the 6284 Å DIB to the small 6196 Å DIB.

Finally, we show in Fig. 15 a weighted mean value of E_{B-V} derived from the three DIBs, again compared with the E_{V-I} value deduced from the OGLE analysis. This figure allows determining to what extent the combination of those three DIBs can be used here as a first estimator for the reddening, in the absence of photometric measurements. The average linear relationship is $E_{B-V} = (0.72 \pm 0.14)\ E_{V-I} + (0.06 \pm 0.10)$ and the standard deviation is 0.08, i.e. on the order of 15% of the average value. This should be compared with other conditions and distances.

7. Summary and discussion

We have used $R = 22\,500$, $S/N = 30$–77 observations of 219 red clump giants from the galactic bulge in Baade's Window ($A_v \simeq 1.4$) as a test case for our newly developed composite

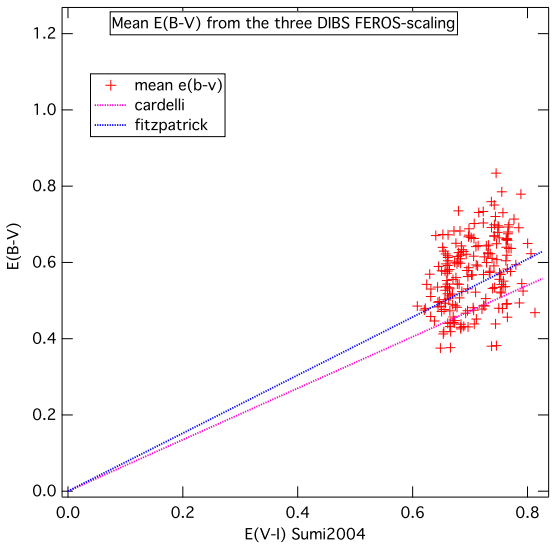

Fig. 15. Synthesis of all E_{B-V}s estimates from the 3 DIBs, in the form of a weighted mean, here compared with the E_{V-I} determination from the OGLE photometry. The blue and pink dotted lines correspond to color excess relationships based on the Fitzpatrick (1999) and Cardelli et al. (1989) extinction curves.

model and automated fitting method of IS absorption extraction from cool star spectra. The combination of synthetic stellar models, synthetic atmospheric lines, and DIB profiles allowed us to extract EW values for the three DIBs 6284, 6196, and 6204 Å. The existence of DIB-DIB correlations demonstrates that, even without any adaptation of the stellar model, in the case of a moderate color excess $E_{B-V} \simeq 0.4$ and of signal-to-noise ratios above 30, a strong DIB like the 6284 Å band, but also narrow and weaker DIBs like the 6196 or the 6204 Å bands, can be measured for cool stars, provided one takes the velocity shift into account between the star and the absorbing ISM. More precisely, all spectra could be efficiently used in the case of the strong and broad 6284 Å DIB (width ≃3.5 Å, depth ≃20%), while for the two narrow and weaker DIBs (≃0.5 and 1 Å width, 10% depth) the potential extraction of the DIB EW depends on the star's radial velocity, whose value results in an overlap of stellar lines and DIBs or does not. This is due to the presence of unidentified lines, as well as to over- or underpredicted line strengths. Model improvements are beyond the scope of this work, but should be performed in future, once other analyses confirm the present trends and enough constraints have been obtained. Here we simply performed an empirical correction, independently for each DIB, which is described in the Appendix. Its validity was demonstrated by a strong improvement in the DIB-DIB correlations, as well as improvements in the DIB-extinction correlations. More work is needed on a more fundamental approach to those corrections. Overall, this modeling demonstrates that DIBs can be measured in an automated way for a large number of cool targets during spectroscopic surveys, and be used as any other IS line to locate the IS matter.

For the three DIBs, the spatial pattern generally reflects extinction variations deduced from stellar photometry, which also validates the fitting method. The degree of correlation is, as expected, generally better for the broader and stronger DIB because uncertainties on the EWs are much smaller. DIB strengths are converted into color excesses, using best-fit linear relationships established for early-type star surveys. Mean values of E_{B-V} over all targets are 0.53, 0.62, and 0.52 for the 6284, 6204, and 6196 Å DIBs, respectively. Discrepancies among the DIBs amount to about 20%, and there is a 15% dispersion of the weighted mean value around its average linear relationship with the photometric reddening (Fig. 15). There were several results from the analysis that call for further studies. The 6284, and to a smaller extent the 6204 Å DIBs amplitude intervals over the field, are found to be larger than the color excess relative variations deduced from OGLE photometric data and their analysis (Sumi 2004, see Fig. 12). This is reflected in the spatial variability of the DIB-based to photometry-based color excess ratio. Those variations are not randomly located, as is especially visible for the 6284 Å DIB: the DIB is systematically weaker around $\alpha, \delta = 270.95, -30°$. One likely explanation for such departures from proportionality is the DIB response to ionization conditions in the clouds and other environmental effects such as shocks.This may be linked to the spatial variability of the extinction law. The grain size distribution influences the shape of the extinction law and the R_v, but it is also linked to the cloud's physical properties and its history, which in turn influence the quantity of macro-molecules and the DIBs. Such a link between the R_v and the DIBs has been discussed by Krełowski et al. (1999). The excess of amplitude variation and the spatial variability do not seem to exist for the small 6196 Å DIB, although large uncertainties make the comparison with the photometric extinction more difficult. This may relate to this DIB having been found to be better correlated with the extinction than the two others, something again potentially related to its different response to the dust distribution, or the environmental conditions. Moreover, the absolute value of the extinction based on the 6196 Å DIB (again deduced from the average solar neighborhood relationship) seems to agree better with the photometric determination than do the two other DIBs.

More analyses should be performed over various fields and for targets at various distances to confirm unidentified or poorly predicted stellar lines. More data should help in refining the stellar models in the DIB spectral regions and subsequently improve the DIB extraction. On the other hand, extinction estimates would certainly be strongly improved by the use of multiple DIBs and of their ratios, accompanied by better understanding of their specific behavior. Such studies may also provide additional information on the links between the extinction law and the DIBs.

Acknowledgements. We thank the referee for the useful comments on the manuscript. H.-C. C. wants to acknowledge the Taiwanese government for her scholarship NSC100-2917-I-564-057.

Appendix A: Error estimates

Estimating uncertainties on the DIB EWs is not straightforward here, as there are different sources of errors. The error linked to measurement uncertainties can in principle be classically estimated. For the 219 spectra of this study, the signal-to-noise ratio varies between from 30 and 77 per pixel. It can be immediately derived that for a broad DIB covering about 6 Å (i.e. defined over more than 100 pixels and of about 10−15% depth, which corresponds to the 6284 Å one), the relative error due to the noise should only be very small. For the shallower and narrower DIBs, this is not the case. The other major source of uncertainties comes from the use of synthetic spectra, which have not been adjusted individually for all targets. As shown by Figs. 6 to 9, those uncertainties may approach the DIB itself depending on the star radial velocity, for the two small DIBs.

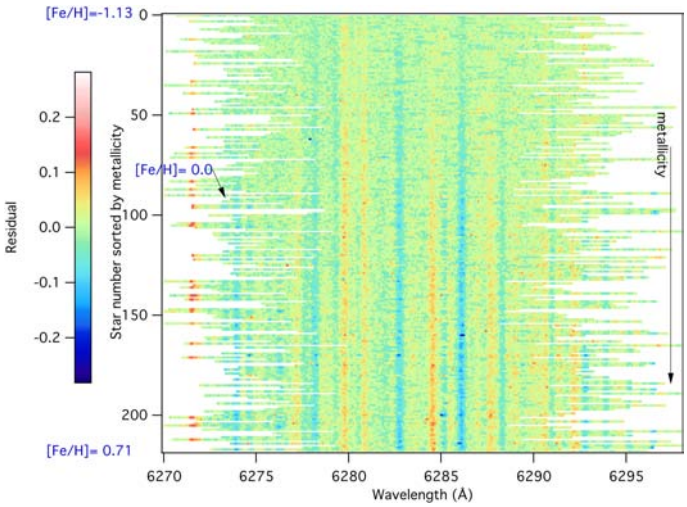

Fig. A.1. Residuals as a function of wavelength and metallicity for the DIB 6283.8 Å. They form the basis for the EW correction and the error estimate.

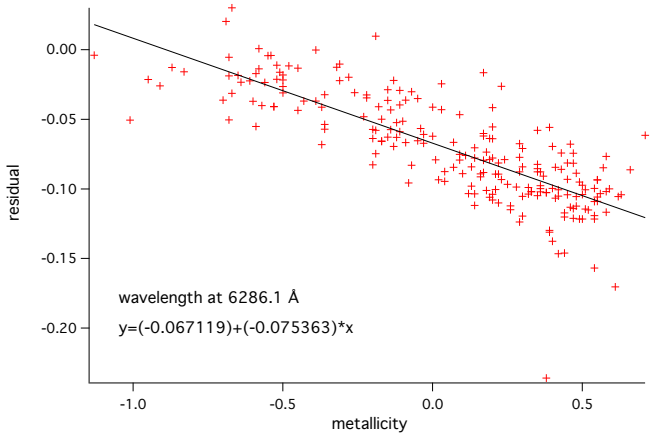

Fig. A.2. Example of residuals vs. -metallicity relationships: here the residuals depend on the metallicity and are negative, which corresponds to an under-predicted stellar absorption line.

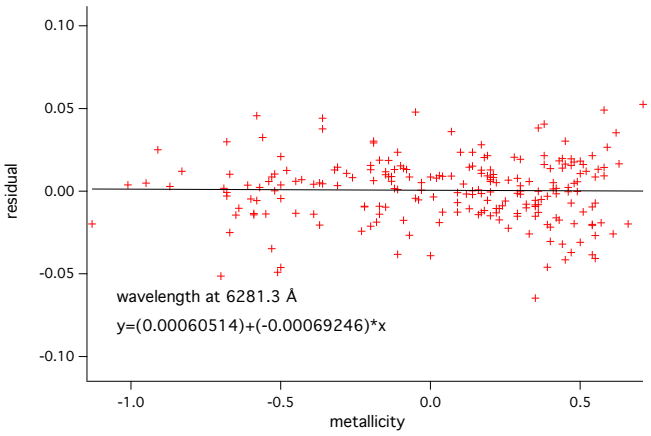

Fig. A.3. Example of residuals vs. -metallicity relationships: here the residuals do not depend on the metallicity and are negligible.

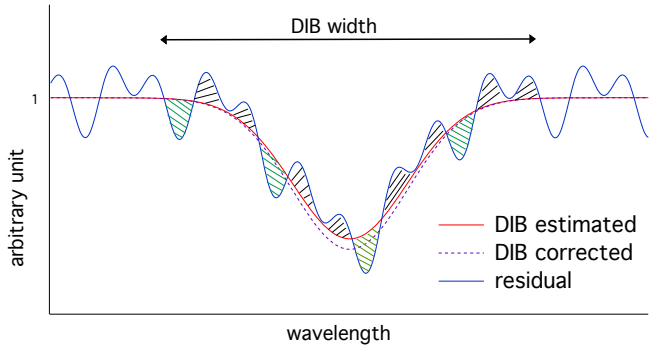

Fig. A.4. Schematic illustration of the correction applied to the EW measurements. The red curve represents the DIB profile as it comes out from the fitting phase. Hatched surfaces show the offsets applied at each wavelength that are computed for each star, as a function of its metallicity. The dashed line illustrates the corrected DIB.

We have devised a method for error estimates that has the advantage of providing a corrective term for the DIB EW in addition to the errors. For each target, the (*data* − *model*) residuals for the best adjustment are shifted into the stellar frame. Those residuals are then sorted by metallicity. The corresponding 2D residual plot is shown in Fig. A.1 for the 6284 Å DIB. The *x*-axis is the wavelength in the star frame, and the *y*-axis is the metallicity. The color scale represents the value of the residuals. Obviously there are some features at specific wavelengths, some quite strong, and they are also obviously related to the metallicity. They correspond to stellar lines that are under- or overpredicted by the synthetic spectra. A large number of lines are simply unidentified. The next step is to use this map in the orthogonal direction, i.e., to extract the residual as a function of the metallicity, for each wavelength in the star frame. Examples of the obtained extracted series are shown in Figs. A.2 and A.3. Each of those metallicity-residual series of points is then fitted to a linear relationship, as shown in the two plots. For the wavelength corresponding to Fig. A.2, the residual is negative, and its absolute value increase strongly with the metallicity. This means that at this location there is a stellar line that is under-predicted and that the higher the metallicity, the greater the data-model discrepancy. At variance with this case, at the wavelength corresponding to Fig. A.3, the residual is on average zero and not related to the metallicity. This means that there is no stellar line at this location, or that the model does predict the line adequately. We then use both the fit coefficients (at each wavelength) to correct the previously computed DIB profile and the standard deviation around the mean relationship (again at each wavelength) to estimate the random (or quasi-random) remaining errors. More precisely, for each star we consider the wavelength interval that contains the entire DIB, and compute for each wavelength the most-probable residual as a function of the star metallicity, based on the linear relationships coefficients. We apply this correction over the whole DIB interval (as shown in Fig. A.4) and recalculate the DIB EW. Table 3 contains both the initial and corrected values for the EW for the three DIBs and all targets. We found that the recalculated EWs provide significantly improved DIB-DIB correlations, which demonstrates that this method provides a partial, but valid correction.

The distribution of data points around the mean residual-metallicity relationship provides an estimate of the combination of unpredictable uncertainties linked to the stellar lines and the actual noise). We then used the standard deviation measured for each relationship to compute the standard deviation at each wavelength, then propagated the errors on the whole DIB interval. In the case of the two narrow DIBs, this estimated uncertainty may be smaller in some cases than the actual errors;

however, considering those deviations as systematic and not random leads to errors that are unrealistically large.

References

Cami, J., Sonnentrucker, P., Ehrenfreund, P., & Foing, B. H. 1997, A&A, 326, 822
Cardelli, J. A., Clayton, G. C., & Mathis, J. S. 1989, ApJ, 345, 245
Clough, S. A., Shephard, M. W., Mlawer, E. J., et al. 2005, J. Quant. Spec. Radiat. Transf., 91, 233
Fitzpatrick, E. L. 1999, PASP, 111, 63
Friedman, S. D., York, D. G., McCall, B. J., et al. 2011, ApJ, 727, 33
Fulara, J., & Krelowski, J. 2000, New Astron. Rev., 44, 581
Galazutdinov, G. A., Lo Curto, G., & Krełowski, J. 2008, MNRAS, 386, 2003
Herbig, G. H. 1995, ARA&A, 33, 19
Hill, V., Lecureur, A., Gómez, A., et al. 2011, A&A, 534, A80
Hobbs, L. M., York, D. G., Snow, T. P., et al. 2008, ApJ, 680, 1256
Hobbs, L. M., York, D. G., Thorburn, J. A., et al. 2009, ApJ, 705, 32
Jenniskens, P., & Desert, F.-X. 1994, A&AS, 106, 39
Krelowski, J., & Walker, G. A. H. 1987, ApJ, 312, 860
Krełowski, J., Ehrenfreund, P., Foing, B. H., et al. 1999, A&A, 347, 235
Kurucz, R. L. 2005, Mem. Soc. Astron. It. Suppl., 8, 14
Lallement, R., Bertin, P., Chassefiere, E., & Scott, N. 1993, A&A, 271, 734
Marshall, D. J., Robin, A. C., Reylé, C., Schultheis, M., & Picaud, S. 2006, A&A, 453, 635
Moore, C. E., Minnaert, M. G. J., & Houtgast, J. 1966, National Bureau of Standards Monograph, Washington: US Government Printing Office (USGPO)
Raimond, S., Lallement, R., Vergely, J. L., Babusiaux, C., & Eyer, L. 2012, A&A, 544, A136
Rothman, L. S., Gordon, I. E., Barbe, A., et al. 2009, J. Quant. Spec. Radiat. Transf., 110, 533
Salama, F., Bakes, E. L. O., Allamandola, L. J., & Tielens, A. G. G. M. 1996, ApJ, 458, 621
Sbordone, L. 2005, Mem. Soc. Astron. It. Suppl., 8, 61
Sbordone, L., Bonifacio, P., Castelli, F., & Kurucz, R. L. 2004, Mem. Soc. Astron. It. Suppl., 5, 93
Snow, T. P., & Destree, J. D. 2011, EAS Publ. Ser., 46, 341
Sumi, T. 2004, MNRAS, 349, 193
Udalski, A. 2003, ApJ, 590, 284
Vos, D. A. I., Cox, N. L. J., Kaper, L., Spaans, M., & Ehrenfreund, P. 2011, A&A, 533, A129

Table 3. Stellar data and measurement of EW.

Star	OgleN	$T_{\rm eff}$ K	log g Dec	ξ km s^{-1}	[Fe/H] Dec	E_{B-V}*	EW(6196) mÅ	Corr'd mÅ	EW(6204) mÅ	Corr'd mÅ	EW(6284) mÅ	Corr'd mÅ
1	67 536	5121	2.43	1.1	−0.45	0.483	40	36 ± 11	164	170 ± 38	1046	1036 ± 62
2	67 610	4865	2.34	1.5	−0.31	0.425	36	33 ± 10	110	111 ± 38	1053	1009 ± 64
3	67 641	4575	2.17	1.4	−0.36	0.445	50	42 ± 13	164	173 ± 38	962	939 ± 64
4	67 663	4878	2.33	1.4	−0.05	0.448	50	46 ± 10	175	179 ± 39	1023	974 ± 64
5	67 675	4507	2.16	1.5	0.42	0.434	49	36 ± 12	87	94 ± 38	991	919 ± 64
6	67 687	4664	2.27	1.5	0.54	0.442	64	57 ± 13	130	130 ± 38	942	909 ± 64
7	67 727	4994	2.45	1.5	0.55	0.45	37	31 ± 10	206	213 ± 38	838	766 ± 64
8	67 744	5170	2.42	1.4	−0.43	0.447	36	34 ± 10	175	172 ± 37	895	891 ± 62
9	67 762	4943	2.34	1.3	−0.26	0.468	21	21 ± 13	131	137 ± 34	884	868 ± 73
10	78 185	4763	2.3	1.2	0.21	0.464	13	24 ± 14	105		840	887 ± 62
11	78 195	4807	2.34	1.1	−0.05	0.419	34	30 ± 13	161	167 ± 38	951	938 ± 62
12	78 202	4460	2.17	1.5	0.54	0.441	19	12 ± 10	88	95 ± 38	924	855 ± 64
13	78 205	5271	2.37	1	0.2	0.473	39	35 ± 10	53	57 ± 38	555	493 ± 64
14	78 215	4738	2.22	1.6	0.55	0.484	38	22 ± 12	53	81 ± 34	747	
15	78 255	4810	2.31	1.4	0.49	0.452	38	40 ± 9	184	177 ± 37	852	871 ± 63
16	78 271	4685	2.21	1.5	0.17	0.428	24	28 ± 11	155	161 ± 38	816	813 ± 62
17	78 281	4899	2.31	1.1	0.2	0.448	32	39 ± 10	179	177 ± 37	945	966 ± 63
18	78 283	4512	2.21	1.5	0.35	0.5	48	47 ± 10	242	235 ± 37	895	918 ± 63
19	78 288	5136	2.3	1.5	−0.48	0.429	27	28 ± 13	126	143 ± 36	800	835 ± 63
20	78 322	4978	2.37	0.8	−0.67	0.472	70	67 ± 10	205	202 ± 37	978	970 ± 63
21	78 323	4867	2.35	1.5	0.3	0.431	27	37 ± 10	131	123 ± 36	799	827 ± 63
22	78 330	4595	2.18	1.5	0.61	0.48	40	47 ± 11	180	185 ± 37	1035	1042 ± 62
23	78 354	4738	2.29	1	0.03	0.442	35	41 ± 10	152	146 ± 36	768	793 ± 63
24	78 357	4620	2.09	1.5	0.37	0.442	29	39 ± 13	136		840	880 ± 63
25	78 379	4775	2.31	1.3	0.03	0.421	34	30 ± 12	131	146 ± 34	960	952 ± 73
26	78 393	4943	2.26	1.2	−0.18	0.465	33	38 ± 10	133	124 ± 34	903	924 ± 63
27	78 401	4851	2.24	1.5	0.14	0.424	11	7 ± 12	140	138 ± 38	818	762 ± 64
28	78 421	4632	2.22	1.5	0.46	0.417	25	28 ± 11	177	177 ± 37	838	849 ± 62
29	78 436	4541	2.19	1.3	0.32	0.43	23	12 ± 13	−21	2 ± 34	802	780 ± 73
30	78 449	4947	2.22	1.7	0.54	0.418	25	30 ± 12	155	154 ± 38	759	758 ± 62
31	78 461	4539	2.16	1.3	0.32	0.442	37	50 ± 11	218	180 ± 36	809	824 ± 63
32	89 573	4819	2.25	1.4	0.35	0.474	44	19 ± 16	74	91 ± 34	885	
33	89 589	4690	2.13	1.5	−0.13	0.414	25	24 ± 12	48	48 ± 38	817	777 ± 67
34	89 590	5151	2.42	1.5	−0.23	0.419	37	53 ± 14	115	120 ± 36	798	854 ± 62
35	89 609	4898	2.29	1.2	−0.15	0.429	35	33 ± 12	149	157 ± 38	915	906 ± 62
36	89 614	4734	2.26	1.5	0.59	0.414	39	46 ± 12	76		784	
37	89 640	4641	2.21	1.5	0.19	0.393	18	17 ± 12	97	99 ± 38	878	872 ± 62
38	89 645	4674	2.22	1.6	0.28	0.416	41	32 ± 13	118	122 ± 38	797	767 ± 64
39	89 667	4516	2.11	1.5	0.66	0.417	53	41 ± 13	78	81 ± 38	783	748 ± 64
40	89 669	4964	2.44	1.4	0.39	0.434	35	47 ± 10	141	113 ± 34	1029	1050 ± 63
41	89 687	4743	2.33	1.5	0.5	0.441	43	40 ± 13	106	105 ± 38	846	822 ± 63
42	89 702	4714	2.2	1.2	0.2	0.436	31	49 ± 14	148	124 ± 36	913	949 ± 62
43	89 731	4784	2.22	1.3	−0.12	0.421	33	31 ± 13	129	137 ± 35	825	803 ± 72
44	89 735	4579	2.07	1	0.11	0.45	36	25 ± 13	111	116 ± 38	976	944 ± 64
45	89 736	4483	2.15	1.4	0.47	0.431	30	50 ± 12	255	210 ± 36	837	850 ± 63
46	89 774	4635	2.13	1.5	0.22	0.44	39	38 ± 10	150	145 ± 37	820	834 ± 62
47	89 786	4705	2.31	1.1	−0.19	0.433	26	23 ± 10	82	84 ± 39	851	803 ± 64
48	89 802	4481	2.12	1.5	0.45	0.458	52	51 ± 10	188	181 ± 37	855	881 ± 62
49	89 832	4546	2.14	1.4	0.17	0.4	25	33 ± 10	150	134 ± 35	757	785 ± 63
50	89 843	5270	2.38	1.1	0.17	0.434	40	53 ± 12	144	116 ± 36	956	972 ± 63
51	89 848	4582	2.08	1.4	0.09	0.434	47	46 ± 10	72		931	
52	89 871	4502	2.17	1.5	0.36	0.428	47	52 ± 11	138	142 ± 37	872	876 ± 62
53	101 453	4966	2.39	1.2	−0.1	0.433	35	34 ± 11	160	167 ± 38	928	920 ± 62
54	101 462	4807	2.25	1.3	0.07	0.433	24	37 ± 13	167	147 ± 36	883	904 ± 63
55	101 470	4567	2.2	1.4	0.62	0.415	5	24 ± 17	22		999	
56	101 476	4838	2.34	1.5	−0.11	0.433	30	43 ± 14	110		802	858 ± 63
57	101 486	4760	2.15	1.3	−0.6	0.419	34	33 ± 10	135	136 ± 35	941	961 ± 63
58	101 505	4584	2.16	1.5	0.17	0.429	44	37 ± 13	164	168 ± 38	884	856 ± 64
59	101 540	4754	2.35	1.5	0.38	0.4	39	39 ± 10	98	94 ± 37	789	803 ± 62
60	101 606	4647	2.08	1.5	0.58	0.399	23	46 ± 12	175	123 ± 36	763	775 ± 63
61	101 638	4556	2.14	1.4	−0.37	0.408	28	27 ± 10	145	140 ± 37	650	654 ± 63
62	101 648	5025	2.33	1.6	−0.07	0.457	31	30 ± 10	124	118 ± 37	708	719 ± 63
63	101 650	4801	2.21	1.5	0.44	0.413	48	46 ± 10	169	162 ± 37	792	815 ± 62

Notes. * E_{B-V} is derived from the Sumi Sumi (2004) by interpolation.

Table 3. continued.

Star	OgleN	$T_{\rm eff}$	log g	ξ	[Fe/H]	E_{B-V}*	EW(6196)	Corr'd	EW(6204)	Corr'd	EW(6284)	Corr'd
		K	Dec	km s^{-1}	Dec		mÅ	mÅ	mÅ	mÅ	mÅ	mÅ
64	101 655	5274	2.46	1.2	0.71	0.399	14	30 ± 14	76	19 ± 36	826	872 ± 62
65	101 662	4465	2.05	1.2	0.29	0.401	12	3 ± 13	80	100 ± 35	757	733 ± 73
66	101 674	4644	2.23	1.5	0.43	0.425	−5	19 ± 14	122	83 ± 36	808	840 ± 62
67	101 681	4763	2.23	1.5	0.36	0.433	22	35 ± 14	82	46 ± 36	654	701 ± 62
68	101 691	4857	2.23	1.6	0.21	0.412	30	30 ± 10	137	134 ± 37	649	658 ± 62
69	101 692	4449	1.99	1.5	0.25	0.41	21	20 ± 12	145	146 ± 38	707	702 ± 62
70	101 703	4931	2.2	1.5	0.16	0.404	41	31 ± 13	99	103 ± 38	691	662 ± 64
71	234 759	4458	2.06	1.5	0.35	0.507	6	31 ± 13	204	169 ± 36	1028	1055 ± 63
72	234 802	4288	1.97	0.8	0.23	0.488	55	64 ± 10	229	202 ± 35	1135	1154 ± 63
73	234 810	4521	2.12	1.2	−0.5	0.5	32	31 ± 10	111	109 ± 39	1054	1016 ± 64
74	234 811	4773	2.28	1.4	−0.39	0.498	24	23 ± 11	81	78 ± 39	1075	1029 ± 64
75	234 849	4556	2.19	1.2	0.2	0.467	57	56 ± 12	188	190 ± 38	961	956 ± 62
76	234 877	4538	2.14	0.8	−0.2	0.467	47	52 ± 10	183	175 ± 34	828	849 ± 63
77	234 898	4714	2.26	0.8	0.18	0.476	44	42 ± 10	167	162 ± 37	984	995 ± 62
78	234 905	5042	2.28	1.3	−0.12	0.478	30	31 ± 9	143	138 ± 37	836	847 ± 63
79	234 917	5050	2.39	1.5	−0.7	0.458	24	16 ± 12	217	234 ± 38	874	859 ± 62
80	234 926	4830	2.3	1.3	−0.68	0.445	36	33 ± 10	140	136 ± 37	934	928 ± 63
81	234 929	4893	2.35	0.8	−0.68	0.483	47	38 ± 13	161	177 ± 38	892	874 ± 62
82	235 017	4798	2.31	1.4	0	0.47	47	43 ± 13	156	162 ± 38	1024	1012 ± 62
83	244 618	4410	2.03	1.4	−0.17	0.463	42	40 ± 10	161	157 ± 37	899	905 ± 63
84	244 635	4650	2.24	1.5	−0.19	0.435	35	39 ± 11	119		855	
85	244 642	4757	2.15	1.5	0.3	0.462	24	34 ± 10	185	166 ± 35	830	859 ± 63
86	244 660	4736	2.17	1.3	−0.28	0.43	44	39 ± 13	139	149 ± 38	890	878 ± 62
87	244 668	4627	2.17	1.5	0.51	0.406	44	62 ± 11	167	119 ± 36	868	880 ± 63
88	244 704	4916	2.22	1.3	−0.14	0.431	31	36 ± 10	156	153 ± 36	989	1012 ± 63
89	244 718	4724	2.29	1.4	0.12	0.417	30	31 ± 9	177	171 ± 37	960	974 ± 63
90	244 727	4641	2.27	1.3	0.35	0.394	36	29 ± 13	107	109 ± 38	823	792 ± 64
91	244 728	4491	2.03	1.5	0.3	0.463	39	50 ± 14	140	112 ± 36	940	987 ± 62
92	244 734	4900	2.26	1.5	0.52	0.452	52	44 ± 11	140	147 ± 39	811	754 ± 64
93	244 742	4735	2.23	1.5	−0.03	0.426	53	51 ± 10	158	153 ± 37	952	959 ± 62
94	244 757	4910	2.23	1.2	−0.53	0.419	29	46 ± 14	107	126 ± 36	857	908 ± 62
95	244 763	4775	2.19	1.5	0.14	0.396	33	33 ± 10	143	136 ± 37	806	822 ± 63
96	244 817	4610	2.11	1.5	0.57	0.439	40	54 ± 10	149	109 ± 35	866	884 ± 63
97	244 840	4605	2.11	1.5	0.45	0.412	21	27 ± 11	156	157 ± 38	916	914 ± 62
98	256 395	4650	2.21	1.6	0.41	0.418	27	27 ± 13	143	142 ± 38	896	892 ± 62
99	256 401	4650	2.29	1.5	0.54	0.415	47	32 ± 13	28	59 ± 34	931	906 ± 73
100	256 570	4843	2.19	1.5	0.56	0.42	32	44 ± 16	97		681	
101	256 579	4737	2.26	1.5	0.36	0.422	17	17 ± 12	115	114 ± 38	699	695 ± 62
102	256 650	4598	2.19	1.5	0.44	0.412	26	30 ± 12	124	123 ± 38	674	672 ± 62
103	267 856	4605	2.2	1.2	0.04	0.419	60	61 ± 11	137	141 ± 37	771	769 ± 62
104	267 862	4686	2.23	1.1	−0.17	0.429	23	28 ± 10	127	119 ± 35	747	771 ± 63
105	267 909	4716	2.16	1.4	0.43	0.416	46	56 ± 14	105	67 ± 36	750	798 ± 62
106	267 912	4781	2.28	1.5	0.38	0.417	44	36 ± 11	132	138 ± 38	797	746 ± 64
107	267 985	4990	2.23	1.4	−0.14	0.411	16	12 ± 11	85	85 ± 39	660	606 ± 64
108	268 000	4568	2.2	1.5	0.19	0.416	31	35 ± 12	29		740	
109	268 011	4696	2.24	1.7	0.4	0.419	36	36 ± 10	126	120 ± 37	751	767 ± 62
110	268 022	4968	2.26	1.5	0.22	0.385	24	27 ± 11	128	131 ± 37	712	714 ± 62
111	268 047	4880	2.34	1.3	0.09	0.437	31	28 ± 10	96	99 ± 38	749	691 ± 64
112	268 068	4837	2.31	1.7	0.3	0.416	39	31 ± 11	144	151 ± 39	767	698 ± 64
113	385 048	4686	2.24	1.2	−0.36	0.486	45	41 ± 11	183	192 ± 38	982	971 ± 62
114	392 992	4907	2.34	1.2	−0.22	0.484	40	44 ± 10	163	156 ± 34	977	998 ± 63
115	393 009	5012	2.32	1.5	−0.68	0.471	33	29 ± 13	176	206 ± 36	1054	1093 ± 63
116	393 012	4540	2.24	1.5	0.48	0.478	64	63 ± 10	181	174 ± 37	1006	1028 ± 62
117	393 024	4786	2.26	1.2	−1.13	0.468	35	48 ± 12	112	103 ± 38	1018	994 ± 65
118	393 026	4804	2.3	1.2	−0.5	0.497	41	42 ± 10	168	171 ± 35	1039	1061 ± 63
119	393 028	4457	2.13	1.4	0.36	0.461	18	14 ± 10	103	109 ± 39	1011	952 ± 64
120	393 030	4574	2.18	1.5	0.35	0.475	53	50 ± 13	163	164 ± 38	987	964 ± 63
121	393 033	4914	2.32	1	−0.5	0.453	43	37 ± 11	213	224 ± 38	976	964 ± 62
122	393 070	4903	2.3	1.6	0.47	0.459	41	37 ± 10	134	141 ± 38	1087	1023 ± 64
123	393 088	4575	2.21	1.5	0.22	0.466	20	41 ± 13	164	137 ± 36	979	1007 ± 63
124	393 091	4641	2.15	1.5	0.47	0.486	34	42 ± 14	142		904	944 ± 62
125	393 111	4546	2.21	1.5	0.23	0.464	31	45 ± 14	157	130 ± 36	1005	1048 ± 62
126	393 117	4931	2.26	0.9	−0.07	0.474	36	40 ± 10	173	172 ± 37	1015	1033 ± 63
127	393 124	4540	2.08	1.5	0.5	0.47	17	46 ± 13	192	147 ± 36	1025	1050 ± 63

Table 3. continued.

Star	OgleN	$T_{\rm eff}$	log g	ξ	[Fe/H]	E_{B-V}*	EW(6196)	Corr'd	EW(6204)	Corr'd	EW(6284)	Corr'd
		K	Dec	km s^{-1}	Dec		mÅ	mÅ	mÅ	mÅ	mÅ	mÅ
128	393 125	4528	2.09	1.4	0.29	0.488	30	24 ± 11	153	159 ± 39	982	929 ± 64
129	393 136	4515	2.11	1.4	0.5	0.461	10	19 ± 14	152		1047	1085 ± 63
130	393 138	5073	2.34	1.4	−0.64	0.473	33	24 ± 13	153	161 ± 38	1020	999 ± 64
131	393 152	4757	2.23	1.3	−0.2	0.47	39	36 ± 12	189	198 ± 38	1019	1009 ± 62
132	393 162	4359	2.05	1.5	0.39	0.492	−15	7 ± 18	161		953	
133	393 229	4868	2.32	1.3	−0.59	0.485	21	29 ± 13	144	138 ± 34	1021	1010 ± 73
134	393 319	4473	2.19	1.4	0.26	0.48	50	40 ± 12	55	58 ± 38	1045	981 ± 64
135	393 339	4972	2.41	1	−0.09	0.473	53	45 ± 12	143	148 ± 38	1007	968 ± 64
136	402 417	4655	2.2	1.2	−0.2	0.486	32	41 ± 13	151	150 ± 36	945	978 ± 63
137	402 421	4822	2.36	1.3	0.19	0.485	37	41 ± 11	169	174 ± 38	990	990 ± 62
138	402 432	4579	2.12	1.5	0.29	0.489	19	39 ± 13	187	155 ± 36	951	977 ± 63
139	402 433	4808	2.24	1.3	−0.19	0.461	36	43 ± 12	149	144 ± 36	989	1010 ± 63
140	402 435	4618	2.25	1.2	0	0.482	29	25 ± 12	112	127 ± 34	951	942 ± 73
141	402 440	4429	2.11	1.3	0.29	0.465	45	43 ± 13	115	116 ± 38	912	904 ± 62
142	402 449	4474	2.18	1.5	0.26	0.471	23	18 ± 10	125	130 ± 38	1042	978 ± 64
143	402 463	5260	2.43	1.2	−0.51	0.476	30	31 ± 10	128	131 ± 35	979	1001 ± 63
144	402 470	4270	1.97	1.2	0.16	0.457	27	35 ± 16	111		902	
145	402 477	4545	2.19	1.5	0.51	0.432	37	49 ± 10	196	175 ± 35	827	859 ± 63
146	402 478	4983	2.35	1.2	−0.53	0.47	36	36 ± 10	143	143 ± 37	917	932 ± 63
147	402 482	4871	2.28	1.3	−0.57	0.478	34	30 ± 10	118	120 ± 39	910	875 ± 64
148	402 502	4818	2.19	1.2	−0.95	0.476	32	32 ± 9	146	146 ± 37	840	846 ± 63
149	402 516	4936	2.2	1.3	−0.65	0.46	27	22 ± 10	130	133 ± 39	791	761 ± 64
150	402 518	5034	2.32	1	−0.87	0.446	39	37 ± 9	133	133 ± 37	858	865 ± 63
151	402 550	4420	2.15	1.5	0.39	0.475	46	38 ± 11	69	76 ± 39	845	772 ± 64
152	402 560	4984	2.37	1.1	−1.01	0.441	35	35 ± 9	146	145 ± 37	825	826 ± 63
153	402 600	5158	2.4	1.3	−0.52	0.421	32	25 ± 12	132	146 ± 38	823	810 ± 62
154	402 621	4913	2.28	1.3	−0.56	0.45	37	35 ± 13	142	164 ± 36	767	804 ± 63
155	402 632	4937	2.32	1.5	0.55	0.439	34	30 ± 10	130	137 ± 39	635	572 ± 64
156	402 641	4775	2.18	1.5	0.49	0.458	23	36 ± 10	120	90 ± 34	782	803 ± 63
157	412 854	5191	2.4	1.4	−0.69	0.419	34	31 ± 10	105	107 ± 39	658	627 ± 64
158	412 889	4717	2.23	1.6	0.42	0.4	39	34 ± 13	108	108 ± 38	665	635 ± 64
159	412 894	5118	2.31	1.5	−0.45	0.427	25	30 ± 12	99	97 ± 34	724	715 ± 73
160	412 898	4871	2.22	1.8	0.07	0.415	22	18 ± 10	126	130 ± 38	627	570 ± 64
161	412 921	4617	2.13	1.5	0.47	0.413	69	79 ± 14	99	60 ± 36	601	647 ± 62
162	412 957	4920	2.23	1.5	−0.54	0.422	21	19 ± 10	105	105 ± 39	604	568 ± 64
163	412 979	4756	2.24	1.5	−0.58	0.424	36	32 ± 10	134	133 ± 37	652	643 ± 62
164	413 012	4869	2.29	1.2	−0.15	0.408	32	36 ± 10	144	143 ± 37	685	704 ± 63
165	413 043	4974	2.24	1.5	0.09	0.446	34	35 ± 10	83		699	
166	413 060	4811	2.29	1.1	−0.37	0.422	29	31 ± 10	136	136 ± 37	724	741 ± 63
167	413 066	4674	2.11	1.5	0.44	0.419	33	33 ± 10	193	186 ± 37	684	709 ± 63
168	423 393	4702	2.28	1.5	0.41	0.408	24	25 ± 10	150	143 ± 37	696	718 ± 63
169	423 398	4351	2.05	1.3	0.42	0.426	35	47 ± 10	182	156 ± 34	646	672 ± 63
170	423 427	4818	2.22	1.5	0.33	0.479	41	30 ± 12	126	132 ± 38	688	646 ± 64
171	423 432	4945	2.36	1.4	−0.55	0.409	36	44 ± 14	119	143 ± 36	727	773 ± 62
172	423 434	4753	2.31	1.5	−0.15	0.502	28	25 ± 12	145	153 ± 38	759	749 ± 62
173	423 461	4743	2.24	1	−0.13	0.48	27	24 ± 12	165	173 ± 38	668	659 ± 62
174	423 485	4779	2.3	1.5	0.1	0.421	11	23 ± 14	108	94 ± 36	692	741 ± 62
175	423 486	5448	2.42	1.3	−0.39	0.483	28	32 ± 13	112	121 ± 36	695	723 ± 63
176	423 511	4472	2.03	1.2	−0.11	0.458	31	36 ± 10	153	147 ± 36	780	805 ± 63
177	423 516	4808	2.18	1.2	0.4	0.472	4	29 ± 13	124	85 ± 36	727	754 ± 63
178	423 530	4922	2.28	1	−0.11	0.415	51	49 ± 10	152	148 ± 37	807	811 ± 62
179	423 539	4676	2.11	1.5	0.54	0.418	36	50 ± 10	144	104 ± 35	774	791 ± 63
180	423 541	4491	2.18	1.4	0.2	0.447	39	34 ± 10	116	120 ± 39	710	649 ± 64
181	423 543	4975	2.4	1.4	−0.91	0.433	32	34 ± 10	87	80 ± 39	684	659 ± 64
182	423 551	4911	2.28	1.5	0.14	0.42	24	19 ± 10	136	141 ± 38	869	811 ± 64
183	423 569	4598	2.18	1.5	0.45	0.442	42	52 ± 10	183	180 ± 37	688	711 ± 63
184	423 573	5164	2.39	1.1	−0.59	0.421	25	24 ± 10	119	120 ± 37	764	780 ± 63
185	423 604	4422	2.07	1.3	0.55	0.422	21	21 ± 13	96	93 ± 38	736	731 ± 62
186	423 876	4671	2.29	1.5	0.02	0.469	36	42 ± 12	105		618	
187	545 299	4483	2.16	1	0.17	0.486	52	48 ± 13	144	147 ± 38	1111	1093 ± 62
188	545 326	4578	2.16	1.1	0.2	0.524	8	20 ± 14	102		1260	1307 ± 63
189	545 421	5012	2.39	1.2	−0.22	0.492	45	49 ± 10	170	162 ± 34	1047	1068 ± 63
190	545 444	4407	2.07	1.5	0.48	0.485	23	15 ± 11	63	69 ± 39	991	936 ± 64

Table 3. continued.

Star	OgleN	$T_{\rm eff}$ K	log g Dec	ξ km s^{-1}	[Fe/H] Dec	E_{B-V}*	EW(6196) mÅ	Corr'd mÅ	EW(6204) mÅ	Corr'd mÅ	EW(6284) mÅ	Corr'd mÅ
191	545 498	4806	2.26	1.5	−0.5	0.484	31	31 ± 10	159	160 ± 37	995	1012 ± 63
192	545 519	4917	2.41	1.5	−0.31	0.483	58	60 ± 10	169		1173	
193	545 749	4556	2.25	1.4	0.04	0.485	44	42 ± 12	155	160 ± 38	1003	995 ± 62
194	554 729	4752	2.28	1.2	−0.83	0.474	41	38 ± 10	162	190 ± 36	997	1025 ± 63
195	554 738	4701	2.32	1.2	0.13	0.511	40	38 ± 10	148	142 ± 37	1007	1020 ± 62
196	554 754	5056	2.3	1.4	−0.52	0.485	41	35 ± 11	191	201 ± 38	949	937 ± 62
197	554 762	4625	2.29	1.4	0.13	0.484	44	45 ± 11	155	157 ± 37	959	960 ± 62
198	554 807	4941	2.4	1.4	−0.04	0.484	32	28 ± 13	92	104 ± 34	887	867 ± 73
199	554 820	4824	2.37	1.5	0.24	0.483	33	22 ± 12	84	99 ± 34	815	
200	554 835	4622	2.17	1.3	0.48	0.455	13	30 ± 17	105		882	
201	554 849	4581	2.19	1.5	0.46	0.47	43	61 ± 12	225	180 ± 36	861	874 ± 63
202	554 860	4877	2.24	1.3	−0.32	0.477	38	32 ± 13	147	157 ± 38	814	802 ± 62
203	554 876	4949	2.38	1.5	−0.03	0.447	29	24 ± 10	131	135 ± 38	748	696 ± 64
204	554 901	4638	2.11	1.2	−0.67	0.45	31	34 ± 12	99	93 ± 38	714	677 ± 64
205	564 834	5356	2.41	1.3	−0.36	0.424	34	32 ± 10	134	130 ± 37	772	773 ± 63
206	564 840	4713	2.23	1.5	0.33	0.435	23	8 ± 12	37	54 ± 34	734	
207	564 857	4912	2.28	1.4	0.01	0.448	21	21 ± 10	122	116 ± 37	695	708 ± 63
208	564 949	4619	2.14	1.5	0.4	0.433	23	45 ± 13	192	153 ± 36	765	787 ± 63
209	564 992	5269	2.37	1.5	−0.61	0.432	30	29 ± 10	142	143 ± 37	685	700 ± 63
210	565 019	4801	2.29	1.5	0.38	0.427	46	36 ± 12	121	127 ± 38	656	611 ± 64
211	565 025	4729	2.19	1.4	−0.58	0.426	32	29 ± 10	118	119 ± 38	629	594 ± 64
212	565 056	5067	2.39	1.6	0.63	0.43	60	68 ± 14	56	2 ± 37	717	766 ± 62
213	565 094	5049	2.32	1.5	0.14	0.515	26	20 ± 13	119	131 ± 35	718	687 ± 71
214	575 390	4639	2.1	1.5	0.18	0.494	40	47 ± 10	147	144 ± 37	692	714 ± 63
215	575 421	4685	2.19	1.2	−0.08	0.477	31	30 ± 10	162	157 ± 37	658	669 ± 63
216	575 448	4583	2.19	1.3	0.58	0.467	39	27 ± 13	25	42 ± 36	675	631 ± 69
217	575 485	4634	2.28	1.1	−0.09	0.483	32	35 ± 9	189	186 ± 37	707	721 ± 63
218	575 542	4636	2.21	1.5	0.58	0.425	24	24 ± 13	124	120 ± 38	703	699 ± 62
219	575 585	4769	2.19	1.2	−0.17	0.441	35	27 ± 12	104	109 ± 38	671	636 ± 64